

The role of VSG parameters in shaping small-signal SG dynamics

Ferdinand Geuss

University of Stuttgart

Stuttgart, Germany

ferdinand.geuss@isys.uni-stuttgart.de

Orcun Karaca

ABB Corporate Research

Baden-Dättwil, Switzerland

orcun.karaca@ch.abb.com

Mario Schweizer

ABB Corporate Research

Baden-Dättwil, Switzerland

mario.schweizer@ch.abb.com

Ognjen Stanojev

ABB Corporate Research

Baden-Dättwil, Switzerland

ognjen.stanojev@ch.abb.com

Abstract—We derive a small-signal transfer function for a system comprising a virtual synchronous generator (VSG), a synchronous generator (SG), and a load, capturing voltage and frequency dynamics. Using this model, we analyze the sensitivity of SG dynamics to VSG parameters, highlighting trade-offs in choosing virtual inertia and governor lag, the limited effect of damper-winding emulation, and several others.

Index Terms—virtual synchronous generator, virtual inertia, grid-forming control

I. INTRODUCTION

As power electronic interfaces become more prevalent, particularly with the renewable integration, the industry increasingly requires advanced grid-forming (GFM) control. These controllers can form voltage, emulate inertia, and realize droop behavior. For such controllers, small-signal methods are widely used especially in single grid-connected converter systems, e.g., with passivity or Nyquist criteria [1]. In contrast, this paper studies the small-signal properties of an interconnected system comprising a converter operated as a virtual synchronous generator (VSG)¹, a synchronous generator (SG), and a load. Unlike the related studies in [2]–[5], the current control and the network dynamics are neglected to focus only on slower dynamics. Such simplified models can reveal behaviors that more detailed models may obscure. This same motivation led to the foundational work in [6], which deliberately overlooked network dynamics to derive a parallel VSG-SG model, unveiling new facets of VSG parametrization. However, that study omits voltage and reactive power dynamics, does not analyze zero locations or their impact, and primarily highlights the benefits of higher inertia/damping and reduced governor delay. These limitations motivate our work, and we address each explicitly.

Among more detailed models, [2] considers simulation studies for a nine-bus system, including the dc-link and current control dynamics, highlighting the interaction between fast GFM control and slow SG dynamics. A small-signal study of parallel VSGs in [3] determines their damping coefficients. In [4], a small-signal model of a VSG-SG interconnection with network dynamics is derived to study low-frequency oscillations using pole plots. They state that increasing the

governor lag and inductance could weaken the influence of the VSG.

Related simplified models are found in [7]–[11]. For example, [7] analyzes instability with grid-following (GFL) penetration; [8] shows damping versus penetration levels; [9] derives a VSG small-signal model highlighting the coupling of QV and $P\omega$ dynamics; [10] studies a GFL converter connected to a VSG; and [11] examines inertia and damping effects in different time intervals during a frequency transient.

The main contribution of this paper is the derivation of a small-signal transfer function mapping load power to internal frequencies and voltages, which we use to analyze the interconnected system with respect to VSG parametrization, in particular, to study the sensitivity of SG dynamics. Compared with [6], the transfer function also captures voltage and reactive power dynamics, and we give specific attention to the locations of its zeros. Section IV shows that these zero locations can significantly affect system behavior. In our analysis, we vary VSG parameters—*inertia*, *damper winding constant*, *governor lag time constant*, *QV-droop gain* and *filter time constant*, *stator inductance*, and *XR-ratio*—one at a time while keeping others at nominal values, to provide insights. These insights either confirm or extend prior findings. For example, we confirm the results of [4] (discussed above), further distinguish oscillations on two distinct time scales, and examine the influence of zeros in both active and reactive power dynamics. Compared with [10], we also confirm the benefits of increased inertia, but we further highlight the advantages of inertia matching. Finally, we validate the transfer function and the main findings through simulation case studies.

II. PRELIMINARIES

Parameters are denoted with upper-case, e.g., K . Bold capitals, e.g., \mathbf{K} , refer to parameter matrices, and K_{ij} describes the entry in the i th row and j th column of \mathbf{K} . The identity is \mathbf{I} . Functions in upper-case refer to transfer functions, e.g., $G(s)$, while transfer function matrices are bold, e.g., $\mathbf{G}(s)$. Here, s is to be interpreted as the derivative operator. Scalar variables are expressed by lower-case, such as v , and their vector versions are denoted bold, e.g., \mathbf{v} . Phasors are marked by an arrow, e.g., $\vec{v} = v \cdot e^{j\varphi} = v\angle\varphi$. Subscripts v , s , b are used to distinguish quantities belonging to the VSG, the SG, and

¹Referring primarily to droop control, inertia, and damper winding emulation functionalities present in GFM.

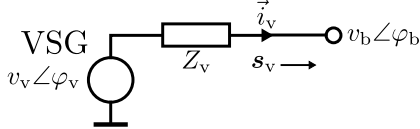


Fig. 1. Diagram of the VSG model.

the bus, respectively. Similarly, references are indicated by the subscript r . For example, the reference frequency is ω_r . For brevity, we often define quantities only for the VSG or only for the SG. Next, we describe the dynamics and the assumptions, and present the interconnected system.

A. VSG Modeling

The VSG dynamics follow [6], with the difference that we include voltage dynamics (see Fig. 1). As in [6], the SG has the same structure as the VSG, with different parametrization. The VSG is modeled as a three-phase voltage source with magnitude v_v and instantaneous phase angle φ_v (i.e., with frequency $\omega_v = s\varphi_v$) in series with a virtual stator impedance Z_v . In contrast to the pure inductances in [6], we have resistive-inductive impedances, i.e., $Z_v = R_v + j\omega_r L_v = R_v + jX_v$. Small-signal changes in the reactance are similarly ignored. The VSG is connected to a bus with magnitude v_b and instantaneous phase angle φ_b (i.e., $\omega_b = s\varphi_b$), and the complex power at the line connecting to this bus is denoted by $s_v = [p_v q_v]^\top$ in vector-form, where p_v and q_v refer to active and reactive power, respectively.

1) *Frequency Dynamics*: The dynamics of ω_v are governed by the swing equation, i.e.,

$$M_v s \omega_v = \frac{p_{v,r} - K_{p,v} (\omega_v - \omega_r)}{1 + T_{p,v} s} - p_v - D_v (\omega_v - \omega_b), \quad (1)$$

with angular momentum M_v , assuming $M_v = J_v \omega_r$. $J_v = \frac{2H_v}{\omega_r^2} S_n$ refers to the moment of inertia, where H_v and S_n are the inertia time constant and the nominal power, respectively.

The first term on the right-hand side of (1), including the power setpoint $p_{v,r}$ and the frequency droop with constant $K_{p,v}$, describes the speed governor. To model the typical delay of the prime mover, a low-pass filter with time constant $T_{p,v}$ is included. For a VSG, $T_{p,v}$ can be lower than that of a real SG. The third term approximates the effect of the damper windings. It is dependent on the difference between internal frequency and bus frequency through a damper winding constant D_v .

2) *Voltage Dynamics*: The voltage dynamics are given by

$$v_v = v_{v,r} + (K_{q,v}/(1 + T_{q,v} s)) (q_{v,r} - q_v). \quad (2)$$

The internal voltage magnitude v_v is determined by QV-droop, i.e., linear around its setpoint $v_{v,r}$ based on the difference between q_v and its setpoint $q_{v,r}$ via the droop constant $K_{q,v}$. Similar to the speed governor, the QV-droop is also subject to delays, modeled by a low-pass filter with time constant $T_{q,v}$.

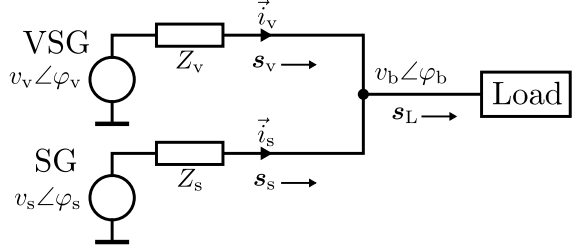


Fig. 2. Diagram of the interconnected system model.

3) *Power Flow*: The quasi-steady state output power supplied to the bus node with voltage \vec{v}_b is given by

$$p_v = \text{Re}\{\vec{v}_b \vec{i}_v^*\} = \frac{R_v (v_v v_b \cos(\theta_v) - v_b^2) + X_v v_v v_b \sin(\theta_v)}{R_v^2 + X_v^2}, \quad (3)$$

$$q_v = \text{Im}\{\vec{v}_b \vec{i}_v^*\} = \frac{X_v (v_v v_b \cos(\theta_v) - v_b^2) - R_v v_v v_b \sin(\theta_v)}{R_v^2 + X_v^2}, \quad (4)$$

where $\theta_v = \varphi_v - \varphi_b$ denotes the angle difference over the stator impedance, also satisfying $s\theta_v = \omega_v - \omega_b$.

B. Setup of the Interconnected System

The VSG, SG, and load are directly connected to a common bus (Fig. 2). The SG and VSG share the same dynamics with different parametrization, and the load power is $s_L = s_v + s_s$. Line impedances between the VSG and SG are assumed negligible. Modeling them would require distinct bus nodes and additional equations, which we relegate to future work.

III. SMALL-SIGNAL DYNAMICS

We first derive a small-signal version of the VSG model, followed by its stand-alone operation and the complete system. For any x , let $x = x_0 + \Delta x$, where x_0 represents the steady-state value (i.e., operating point), while Δx denotes the perturbation variable. Small-signal representation of (1) is:

$$M_v s \Delta \omega_v = -(K_{p,v}/(1 + T_{p,v} s)) \Delta \omega_v - \Delta p_v - D_v (\Delta \omega_v - \Delta \omega_b). \quad (5)$$

Similarly, the small-signal representation of (2) is

$$\Delta v_v = -(K_{q,v}/(1 + T_{q,v} s)) \Delta q_v. \quad (6)$$

Notice that (3) and (4) are nonlinear. To this end, we linearize (3) and (4) with respect to θ_v , v_v , and v_b . Separating operating points and perturbation variables, we get

$$\Delta s_v = [\Delta p_v \Delta q_v]^\top = \mathbf{K}_v [\Delta \theta_v \Delta v_v \Delta v_b]^\top, \quad (7)$$

with the power flow matrix \mathbf{K}_v as in (8) (provided on top of the next page). Finally, we have

$$\Delta \theta_v = \Delta \varphi_v - \Delta \varphi_b, \quad s \Delta \theta_v = \Delta \omega_v - \Delta \omega_b, \quad (9)$$

to describe the relative angle difference and its derivative.

$$\mathbf{K}_v = \begin{bmatrix} \frac{-R_v v_{v,0} v_{b,0} \sin(\theta_{v,0}) + X_v v_{v,0} v_{b,0} \cos(\theta_{v,0})}{R_v^2 + X_v^2} & \frac{R_v v_{b,0} \cos(\theta_{v,0}) + X_v v_{b,0} \sin(\theta_{v,0})}{R_v^2 + X_v^2} & \frac{R_v (v_{v,0} \cos(\theta_{v,0}) - 2v_{b,0}) + X_v v_{v,0} \sin(\theta_{v,0})}{R_v^2 + X_v^2} \\ \frac{-R_v v_{v,0} v_{b,0} \cos(\theta_{v,0}) - X_v v_{v,0} v_{b,0} \sin(\theta_{v,0})}{R_v^2 + X_v^2} & \frac{-R_v v_{b,0} \sin(\theta_{v,0}) + X_v v_{b,0} \cos(\theta_{v,0})}{R_v^2 + X_v^2} & \frac{-R_v v_{v,0} \sin(\theta_{v,0}) + X_v (v_{v,0} \cos(\theta_{v,0}) - 2v_{b,0})}{R_v^2 + X_v^2} \end{bmatrix} \quad (8)$$

A. Stand-Alone VSG Dynamics

We obtain a small-signal transfer function for Figure 1 as

$$[\Delta\omega_v \ \Delta v_v]^\top = \mathbf{G}_v(s) \Delta s_v.$$

We first need to eliminate Δv_b from (7) and $\Delta\omega_b$ from (5) to relate the internal VSG dynamics only to the perturbation variables of power: Δp_v and Δq_v .

To this end, the following is obtained by solving each row of (7) for $\Delta\theta_v$ and eliminating $\Delta\theta_v$:

$$\frac{\Delta p_v - K_{v,12} \Delta v_v - K_{v,13} \Delta v_b}{K_{v,11}} = \frac{\Delta q_v - K_{v,22} \Delta v_v - K_{v,23} \Delta v_b}{K_{v,21}}.$$

Solving for Δv_b yields

$$\begin{aligned} \Delta v_b &= [A_{p,v} \ A_{q,v} \ A_{v,v}] [\Delta p_v \ \Delta q_v \ \Delta v_v]^\top, \quad (10) \\ A_{p,v} &= -\frac{K_{v,21}}{K_{v,11} K_{v,23} - K_{v,13} K_{v,21}}, \\ A_{q,v} &= \frac{K_{v,11}}{K_{v,11} K_{v,23} - K_{v,13} K_{v,21}}, \\ A_{v,v} &= \frac{K_{v,12} K_{v,21} - K_{v,11} K_{v,22}}{K_{v,11} K_{v,23} - K_{v,13} K_{v,21}}. \end{aligned}$$

To eliminate $\Delta\omega_b$ from (5), bring in the following from (7):

$$s \Delta p_v = [K_{v,11} \ K_{v,12} \ K_{v,13}] s [\Delta\theta_v \ \Delta v_v \ \Delta v_b]^\top.$$

Inserting (9) and (10) into the equation above, we get

$$\begin{aligned} s \Delta p_v &= K_{v,11} (\Delta\omega_v - \Delta\omega_b) + K_{v,12} s \Delta v_v \\ &\quad + K_{v,13} (A_{p,v} s \Delta p_v + A_{q,v} s \Delta q_v + A_{v,v} s \Delta v_v). \end{aligned}$$

By reorganizing the terms above, we obtain

$$\begin{aligned} \Delta\omega_v - \Delta\omega_b &= \frac{1 - K_{v,13} A_{p,v}}{K_{v,11}} s \Delta p_v - \frac{K_{v,13} A_{q,v}}{K_{v,11}} s \Delta q_v \\ &\quad - \frac{K_{v,12} + K_{v,13} A_{v,v}}{K_{v,11}} s \Delta v_v. \quad (11) \end{aligned}$$

Towards our goal, we can now substitute (11) into (5), yielding

$$\begin{aligned} M_v s \Delta\omega_v &= - \left(1 + D_v \frac{1 - K_{v,13} A_{p,v}}{K_{v,11}} s \right) \Delta p_v - \frac{K_{p,v}}{1 + T_{p,v} s} \Delta\omega_v \\ &\quad + D_v \frac{K_{v,13} A_{q,v}}{K_{v,11}} s \Delta q_v + D_v \frac{K_{v,12} + K_{v,13} A_{v,v}}{K_{v,11}} s \Delta v_v. \end{aligned}$$

Finally, invoking (6), we get the following for $\Delta\omega_v$:

$$\begin{aligned} \Delta\omega_v &= - \frac{1 + \frac{D_v}{K_{v,11}} (1 - K_{v,13} A_{p,v}) s}{M_v s + \frac{K_{p,v}}{1 + T_{p,v} s}} \Delta p_v \\ &\quad + \frac{\frac{D_v}{K_{v,11}} \left(K_{v,13} A_{q,v} - \frac{K_{q,v}}{1 + T_{q,v} s} (K_{v,12} + K_{v,13} A_{v,v}) \right)}{M_v s + \frac{K_{p,v}}{1 + T_{p,v} s}} s \Delta q_v. \end{aligned}$$

The voltage dynamics are governed by (6). Hence, the small-signal transfer function for stand-alone VSG operation is

$$\begin{aligned} \mathbf{G}_v(s) &= \begin{bmatrix} G_{v,11}(s) & G_{v,12}(s) \\ 0 & -\frac{K_{q,v}}{1 + T_{q,v} s} \end{bmatrix}, \\ G_{v,11}(s) &= -\frac{1 + \frac{D_v}{K_{v,11}} (1 - K_{v,13} A_{p,v}) s}{M_v s + \frac{K_{p,v}}{1 + T_{p,v} s}}, \\ G_{v,12}(s) &= \frac{\frac{D_v}{K_{v,11}} \left(K_{v,13} A_{q,v} - \frac{K_{q,v}}{1 + T_{q,v} s} (K_{v,12} + K_{v,13} A_{v,v}) \right)}{M_v s + \frac{K_{p,v}}{1 + T_{p,v} s}} s. \end{aligned}$$

Analogously, but with a different parametrization, $\mathbf{G}_s(s)$ can be obtained for the SG, satisfying

$$[\Delta\omega_s \ \Delta v_s]^\top = \mathbf{G}_s(s) \Delta s_s.$$

This is omitted in the interest of space.

B. Interconnected System Dynamics

Next, we derive the small-signal transfer function for the complete interconnected system as depicted in Figure 2. These transfer functions are of the following form:

$$\begin{aligned} \Delta y_v &= [\Delta\omega_v \ \Delta v_v]^\top = \mathbf{H}_{L \rightarrow v}(s) \Delta s_L, \\ \Delta y_s &= [\Delta\omega_s \ \Delta v_s]^\top = \mathbf{H}_{L \rightarrow s}(s) \Delta s_L. \end{aligned}$$

Similar to the stand-alone operation, the derivation steps for VSG and SG are analogous. Given the focus of our sensitivity analysis, we present $\mathbf{H}_{L \rightarrow s}(s)$.

Defining $\Delta y_b = [\Delta\omega_b \ \Delta v_b]^\top$, our approach relies on an intermediate step by deriving

$$\begin{aligned} \Delta s_v &= \mathbf{F}_{b,v}(s) \Delta y_b, \\ \Delta s_s &= \mathbf{F}_{b,s}(s) \Delta y_b, \end{aligned}$$

to then isolate either of the VSG or SG dynamics via elimination of certain terms by substitution.

1) *Intermediate Step:* Multiplying both sides of (7) by s , substituting (9), and separating terms dependent on $\Delta\omega_v$ and Δv_v from terms dependent on $\Delta\omega_b$ and Δv_b results in

$$s \Delta s_v = \mathbf{K}_v \begin{bmatrix} \Delta\omega_v - \Delta\omega_b \\ s \Delta v_v \\ s \Delta v_b \end{bmatrix} = \mathbf{B}_{v,v}(s) \Delta y_v + \mathbf{B}_{b,v}(s) \Delta y_b, \quad (12)$$

$$\mathbf{B}_{v,v}(s) = \begin{bmatrix} K_{v,11} & K_{v,12}s \\ K_{v,21} & K_{v,22}s \end{bmatrix}, \quad \mathbf{B}_{b,v}(s) = \begin{bmatrix} -K_{v,11} & K_{v,13}s \\ -K_{v,21} & K_{v,23}s \end{bmatrix}.$$

For the SG, we have the following version of the above:

$$s \Delta s_s = \mathbf{K}_s \begin{bmatrix} \Delta\omega_s - \Delta\omega_b \\ s \Delta v_s \\ s \Delta v_b \end{bmatrix} = \mathbf{B}_{s,s}(s) \Delta y_s + \mathbf{B}_{b,s}(s) \Delta y_b. \quad (13)$$

$B_{s,s}(s)$ and $B_{b,s}(s)$ are omitted in the interest of space.

We can now obtain Δs_v in terms of Δy_b . Inserting $\Delta y_v = G_v(s)\Delta s_v$ into (12) and solving for Δs_v yields

$$\Delta s_v = F_{b,v}(s)\Delta y_b, \quad (14)$$

where $F_{b,v}(s) = (sI - B_{v,v}(s)G_v(s))^{-1}B_{b,v}(s)$. A similar expression can also be obtained for the SG as follows:

$$\Delta s_s = F_{b,s}(s)\Delta y_b, \quad (15)$$

where $F_{b,s}(s) = (sI - B_{s,s}(s)G_s(s))^{-1}B_{b,s}(s)$.

2) *Complete Transfer Function for the SG*: We derive the small-signal transfer function $H_{L \rightarrow s}(s)$ from Δs_L to Δy_s . Inserting inverse of (15) into (13) results in

$$s\Delta s_s = B_{s,s}(s)\Delta y_s + B_{b,s}(s)F_{b,s}^{-1}(s)\Delta s_s,$$

and solving for Δs_s gives

$$\Delta s_s = \left(sI - B_{b,s}(s)F_{b,s}^{-1}(s) \right)^{-1} B_{s,s}(s)\Delta y_s. \quad (16)$$

Notice that if we can relate Δs_s to Δs_L , the derivation is complete. To this end, insert (14) and (15) into $\Delta s_L = \Delta s_v + \Delta s_s$, and then substitute inverse (15) to eliminate Δy_b :

$$\Delta s_L = (F_{b,v}(s) + F_{b,s}(s))F_{b,s}^{-1}(s)\Delta s_s. \quad (17)$$

Combine (16) and (17) to obtain $\Delta y_s = H_{L \rightarrow s}(s)\Delta s_L$:

$$H_{L \rightarrow s}(s) = \left((F_{b,v}(s) + F_{b,s}(s))F_{b,s}^{-1}(s) \right. \\ \left. \times \left(sI - B_{b,s}(s)F_{b,s}^{-1}(s) \right)^{-1} B_{s,s}(s) \right)^{-1}. \quad (18)$$

Remark. The same method also applies when deriving the transfer function $H_{L \rightarrow v}(s)$ for the VSG. The final result is

$$H_{L \rightarrow v}(s) = \left((F_{b,v}(s) + F_{b,s}(s))F_{b,v}^{-1}(s) \right. \\ \left. \times \left(sI - B_{b,v}(s)F_{b,v}^{-1}(s) \right)^{-1} B_{v,v}(s) \right)^{-1}.$$

IV. SENSITIVITY ANALYSIS

This section analyzes the sensitivity of SG dynamics in the interconnected system to variations of VSG parameters. All quantities are per-unit except time, frequency, and angles. Bases are: nominal power of SG/VSG $S_n = 1$ MVA, base voltage $V_n = 6.6$ kV (phase-phase RMS), and nominal frequency $\omega_n = 2\pi 60$ rad/s, $\omega_r = \omega_n$. Parameters largely follow [6], except we adopt a large SG delay $T_{p,s}$ to reflect typically slow SG governors and prime movers [4], [7]. This base case is listed in Table I. The VSG's default damper-winding constant is larger than the SG's, and all remaining parameters match. As in [6], the SG and VSG include no stator resistance in the base case. Later, we vary the VSG's XR-ratio.

Power flow matrices K_v and K_s are dependent on the operating point $v_{v,0}$, $v_{s,0}$, $v_{b,0}$, $\theta_{v,0}$, and $\theta_{s,0}$, obtained by solving the power flow equations (3) and (4). We set $p_{v,0} = p_{s,0} = 0.5$ pu, $q_{v,0} = q_{s,0} = 0.5$ pu, and $v_{b,0} = 1$ pu.

TABLE I
DEFAULT PARAMETERS FOR THE SENSITIVITY ANALYSES.

	VSG	SG
Inertia constant H .	4.0 s	4.0 s
Damper winding constant D .	17 pu	3 pu
Frequency droop K_p .	20 pu	20 pu
Governor lag T_p .	1.0 s	1.0 s
QV droop K_q .	0.1 pu	0.1 pu
QV droop lag T_q .	0.1 s	0.1 s
Stator resistance R .	0.0 pu	0.0 pu
Stator reactance X .	0.2 pu	0.2 pu

TABLE II
OPERATING POINT FOR THE SENSITIVITY ANALYSES.

$v_{v,0}$	1.1045 pu	$\theta_{v,0}$	0.0907 rad
$v_{s,0}$	1.1045 pu	$\theta_{s,0}$	0.0907 rad
$v_{b,0}$	1.0000 pu		

The resulting steady-state voltages and angles are in Table II. Sensitivity results have also been checked at other set points with similar observations. All transfer functions are stable with large margins, so further details are omitted.

A. Sensitivity With Respect to H_v

The inertia constant is varied within [2, 8] s. Fig. 3 shows poles and zeros for all four partial transfer functions of $H_{L \rightarrow s}(s)$ in (18). These four transfer functions are always referred to as $P \rightarrow \omega$, $Q \rightarrow \omega$, $P \rightarrow V$, and $Q \rightarrow V$ in the following, i.e.,

$$H_{L \rightarrow s}(s) = \begin{bmatrix} P \rightarrow \omega & Q \rightarrow \omega \\ P \rightarrow V & Q \rightarrow V \end{bmatrix}.$$

The base case in Table I is plotted in black. Shades of red and blue denote smaller and larger inertia, respectively. Step responses are shown in Fig. 4. Step responses use $\Delta p_L = \Delta q_L = 0.05$ pu. For visualizations, pole-zero pairs are canceled in plots using MATLAB's minreal with tolerance 0.001.

1) *Observations on the Base Case*: In the base case plotted in black, $P \rightarrow \omega$ and $Q \rightarrow \omega$ show a slow resonant pole pair (here referred to as the *primary pole pair*), resulting in a slow oscillatory behavior in the step response. All four transfer functions also exhibit a fast resonant pole pair (here called the *secondary pole pair*), which is partially canceled up to varying degree by accompanying zeros, except in $P \rightarrow V$. Because of incomplete pole-zero cancellation, these faster oscillations are superimposed on the step response of $P \rightarrow \omega$ and $Q \rightarrow \omega$. The cancellation is close to being perfect in $Q \rightarrow V$.

2) *Observations on Inertia*: As Figs. 3 and 4 show, increasing H_v leads to a better damping ratio and a decline of the natural frequency of the primary pole pair for $P \rightarrow \omega$ and $Q \rightarrow \omega$, reconfirming related observations in [6], [7], [10], [12]. For $H_v \neq H_s$, the primary pole pair is also present in $P \rightarrow V$.

By contrast, the secondary poles shift to lower natural frequency and reduced damping for larger H_v , consistent

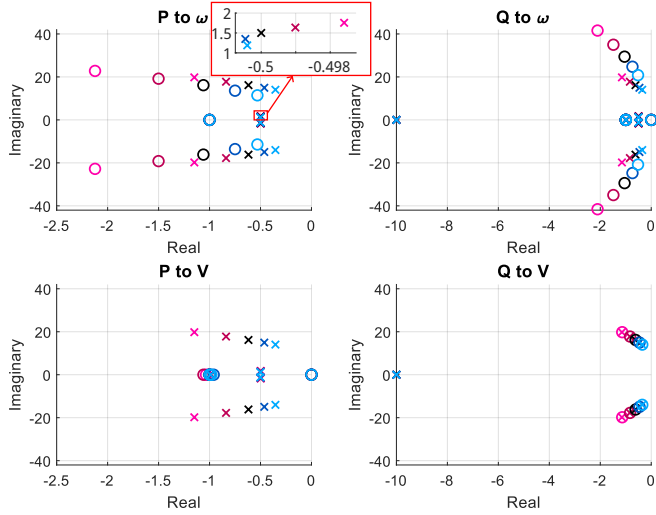


Fig. 3. Pole-zero plots for inertia constants in the range $H_v \in [2, 8]$ s. (Black: base case $H_v = 4$ s, red: H_v smaller than default, blue: H_v larger than default. Darker shades refer to parameter values closer to the base case. Crosses refer to poles, circles indicate zeros.)

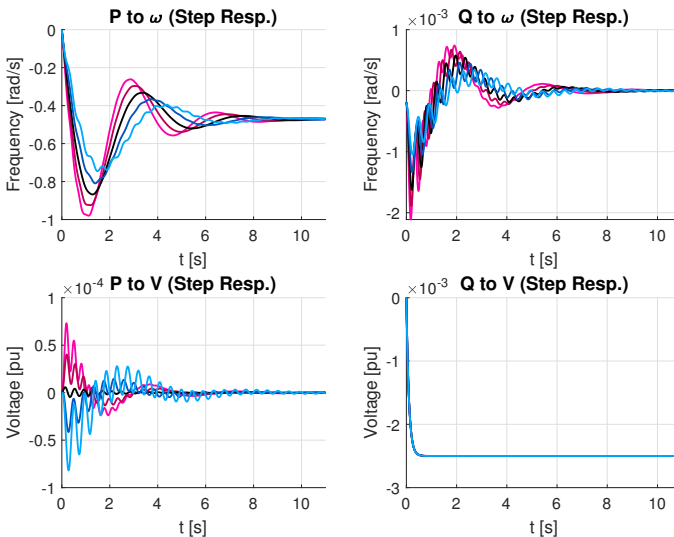


Fig. 4. Step response plots for inertia constants in the range $H_v \in [2, 8]$ s. (Black: base case $H_v = 4$ s, red: H_v smaller than default, blue: H_v larger than default. Darker shades refer to parameter values closer to the base case.)

with transient damping observations for inertialess droop controllers [13]. Zero-pole cancellation is best (in terms of natural frequency) when $H_v = H_s$. Accordingly, the step response of $P \rightarrow \omega$ shows the smallest superimposed secondary oscillations at $H_v = H_s$. Thus, changes in pole-zero cancellation with H_v can affect dynamics as much as pole locations.

$Q \rightarrow \omega$ exhibits primary oscillations that decrease with larger H_v , similar to $P \rightarrow \omega$. Secondary oscillations are slower to decay as H_v increases. $P \rightarrow V$ contains large real zeros for $H_v \neq H_s$, which are omitted in Fig. 3 for clarity, and which grow in magnitude for increasing mismatch, yielding stronger primary and secondary oscillations.

In $Q \rightarrow V$, secondary resonant poles are effectively can-

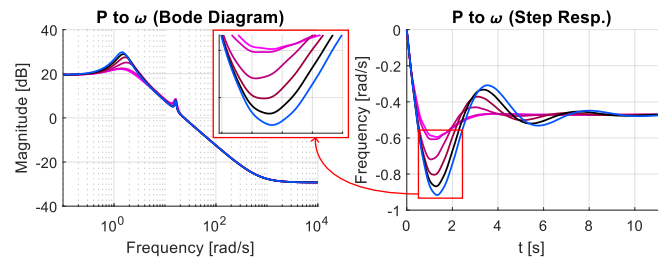


Fig. 5. Bode magnitude plots and step responses of $P \rightarrow \omega$ for $T_{p,v} \in [0.03, 1.3]$ s. (Black: base case $T_{p,v} = 1$ s, red: $T_{p,v}$ smaller than default, blue: $T_{p,v}$ larger than default. Darker shades refer to parameter values closer to the base case.)

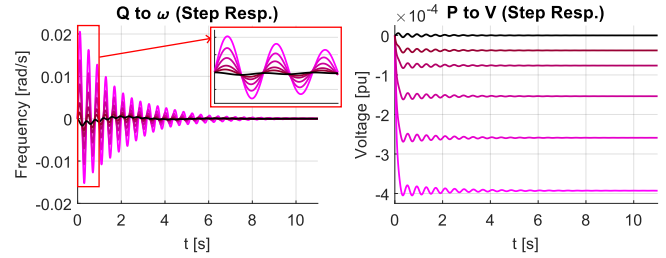


Fig. 6. Step responses plots of $Q \rightarrow \omega$ and $P \rightarrow V$ for various X_v/R_v -ratios. (Black: base case $X_v/R_v = \infty$, red: $X_v/R_v \in [2, 20]$. Darker shades refer to larger ratios.)

celed and the real pole is insensitive to H_v . $Q \rightarrow \omega$ and $P \rightarrow V$ are at least an order of magnitude smaller than $P \rightarrow \omega$ and $Q \rightarrow V$ due to the base case not including stator resistances.

B. Sensitivity With Respect to $T_{p,v}$

Bode diagrams and step responses of $P \rightarrow \omega$ for VSG governor-lag variations $T_{p,v} \in [0.03, 1.3]$ s (nominal $T_{p,v} = 1$ s) are shown in Fig. 5. Increasing $T_{p,v}$ strengthens primary oscillations, whereas small $T_{p,v}$ effectively damps them, consistent with [4, §3.C], [6]. Conversely, secondary oscillations decrease with larger $T_{p,v}$, revealing a trade-off. $Q \rightarrow V$ is largely unaffected by $T_{p,v}$, and is omitted.

C. Sensitivity With Respect to the XR-ratio

Fig. 6 shows step responses of $Q \rightarrow \omega$ and $P \rightarrow V$ for $X_v/R_v \in \{2, 3, 5, 10, 20, \infty\}$; X_v is fixed at its default and R_v is varied. $P \rightarrow \omega$ is unaffected over this range. Although not plotted, $Q \rightarrow V$ shows stronger secondary oscillations for smaller X_v/R_v . In general, $Q \rightarrow \omega$ and $P \rightarrow V$ oscillations grow as X_v/R_v decreases. For $Q \rightarrow \omega$, secondary oscillations become dominant at small X_v/R_v , making primary oscillations negligible. A similar observation has also been provided in [4, §3.C] showing that decreasing the XR-ratio of VSG weakens the damping of low frequency oscillations. For $P \rightarrow V$, the XR-ratio also shifts the steady-state value and a smaller ratio yields slightly larger secondary oscillations.

D. Additional Results

In this section, we list studies relegated to the appendix. Some of the main findings are later highlighted in Section V.

Appendix A provides Bode magnitude plots for sensitivity with respect to H_v and an alternative base case with matched damper winding constants for the SG and VSG. It also includes sensitivities to D_v , $K_{q,v}$, $T_{q,v}$, and X_v . Finally, Appendix B validates the analytical model of Section III and the major observations via simulation case studies.

V. CONCLUSION

We derived a small-signal model to analyze how the VSG parameters influence the SG dynamics. Our main findings from the sensitivity analysis are: (i) For inertia, there is a trade-off between suppressing primary oscillations by choosing larger values and increasing secondary oscillations when deviating from $H_v = H_s$. (ii) A larger damper winding constant reduces secondary oscillations but is not effective in damping primary ones. (iii) Matched impedance for VSG and SG yields smaller secondary oscillations. (iv) Smaller governor lag strongly reduces primary oscillations, even though this might induce slightly stronger secondary oscillations. (v) No negative effects from mismatch in QV-droop are observed. Stator impedance and QV-droop control together how the voltage reacts to a change in reactive power. (vi) The magnitude of oscillations grow with decreasing XR-ratio of VSG.

REFERENCES

- [1] L. Harnefors, X. Wang, A. G. Yépés, and F. Blaabjerg, “Passivity-based stability assessment of grid-connected vscs—an overview,” *IEEE JESTPE*, vol. 4, no. 1, pp. 116–125, 2015.
- [2] A. Tayyebi, D. Groß, A. Anta, F. Kupzog, and F. Dörfler, “Frequency stability of synchronous machines and grid-forming power converters,” *IEEE JESTPE*, vol. 8, no. 2, pp. 1004–1018, 2020.
- [3] P. Sun, J. Yao, Y. Zhao, X. Fang, and J. Cao, “Stability assessment and damping optimization control of multiple grid-connected virtual synchronous generators,” *IEEE Trans. on Energy Convers.*, vol. 36, no. 4, pp. 3555–3567, 2021.
- [4] H. Liu, D. Sun, P. Song, X. Cheng, F. Zhao, and Y. Tian, “Influence of virtual synchronous generators on low frequency oscillations,” *CSEE J. of Power and Energy Sys.*, vol. 8, no. 4, pp. 1029–1038, 2022.
- [5] N. Pogaku, M. Prodanovic, and T. C. Green, “Modeling, analysis and testing of autonomous operation of an inverter-based microgrid,” *IEEE Trans. on Power Elec.*, vol. 22, no. 2, pp. 613–625, 2007.
- [6] J. Liu, Y. Miura, and T. Ise, “Comparison of dynamic characteristics between virtual synchronous generator and droop control in inverter-based distributed generators,” *IEEE Trans. on Power Elec.*, vol. 31, no. 5, pp. 3600–3611, 2016.
- [7] Y. Lin, B. Johnson, V. Gevorgian, V. Purba, and S. Dhopde, “Stability assessment of a system comprising a single machine and inverter with scalable ratings,” in *NAPS*, 2017, pp. 1–6.
- [8] R. H. Lasseter, Z. Chen, and D. Pattabiraman, “Grid-forming inverters: A critical asset for the power grid,” *IEEE JESTPE*, vol. 8, no. 2, pp. 925–935, 2019.
- [9] H. Wu, X. Ruan, D. Yang, X. Chen, W. Zhao, Z. Lv, and Q.-C. Zhong, “Small-signal modeling and parameters design for virtual synchronous generators,” *IEEE Trans. on Ind. Elec.*, vol. 63, no. 7, pp. 4292–4303, 2016.
- [10] S. D’Arco and J. A. Suul, “Small-signal analysis of an isolated power system controlled by a virtual synchronous machine,” in *IEEE PEMC*, 2016, pp. 462–469.
- [11] D. Li, Q. Zhu, S. Lin, and X. Bian, “A self-adaptive inertia and damping combination control of vsg to support frequency stability,” *IEEE Trans. on Energy Convers.*, vol. 32, no. 1, pp. 397–398, 2016.
- [12] A. E. Leon and J. M. Mauricio, “Virtual synchronous generator design to improve frequency support of converter-interfaced systems,” *IEEE Trans. on Energy Convers.*, 2024.
- [13] X. He, S. Pan, and H. Geng, “Transient stability of hybrid power systems dominated by different types of grid-forming devices,” *IEEE Trans. on Energy Convers.*, vol. 37, no. 2, pp. 868–879, 2021.

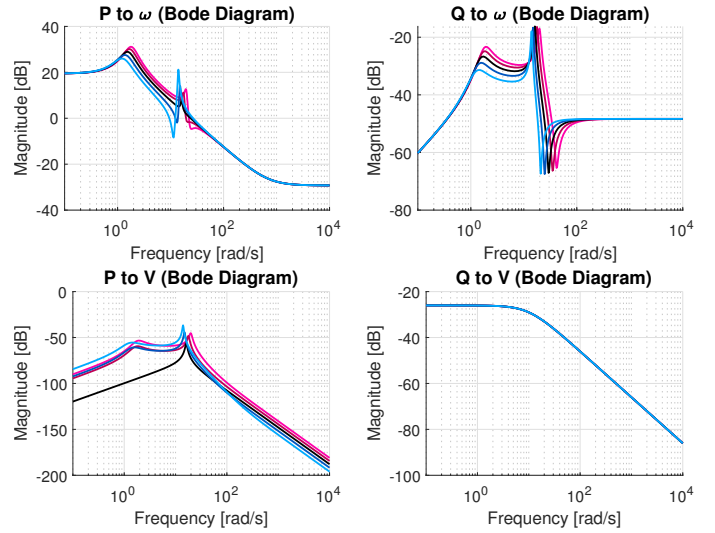


Fig. 7. Bode magnitude plots for inertia constants in the range $H_v \in [2, 8]$ s. (Black: base case $H_v = 4$ s, red: H_v smaller than default, blue: H_v larger than default. Darker shades refer to parameter values closer to the base case.)

APPENDIX A ADDITIONAL SENSITIVITY ANALYSES

A. Sensitivity With Respect to H_v

Bode magnitude plots are provided in Fig. 7.

B. Base Case With Matching Damper Winding Constants

When all the parameters including the damper winding constant are matched between the VSG and the SG, the secondary poles and zeros completely vanish from all partial transfer functions and $P \rightarrow V$ fully reduces to 0. The resulting pole-zero plots are provided in Fig. 8. The primary poles remain unaffected. Hence, the matched parameters case yields a less complex dynamics structure free from any secondary dynamics.

C. Sensitivity With Respect to D_v

Fig. 4 shows that larger inertia yields stronger secondary oscillations. Hence, larger inertia $H_v = 2H_v^{\text{default}}$ is chosen such that the effect of variations in D_v is more pronounced. $Q \rightarrow V$ is insensitive to changes in D_v . Thus, Fig. 9 provides only the Bode plots and step responses of $P \rightarrow \omega$ for damper winding constants in $[0.3, 34]$ pu, where $D_v = 17$ pu by default. D_v has no effect on the primary resonant poles, and the primary oscillations remain intact. The secondary oscillations decrease for larger damper winding constants. While the degree of pole-zero cancellation does not change with D_v , the pole damping increases with growing D_v .

D. Sensitivity With Respect to $K_{q,v}$

We again use H_v from Table I. Varying $K_{q,v}$ within $[0.05, 0.2]$ pu (default: $K_{q,v} = 0.1$ pu) has virtually no effect on the dynamics of $P \rightarrow \omega$. Thus, Fig. 10 only shows $Q \rightarrow V$. The dynamic behaviour of $Q \rightarrow V$ remains mostly unaffected by the changes in $K_{q,v}$, and only the steady-state value differs.

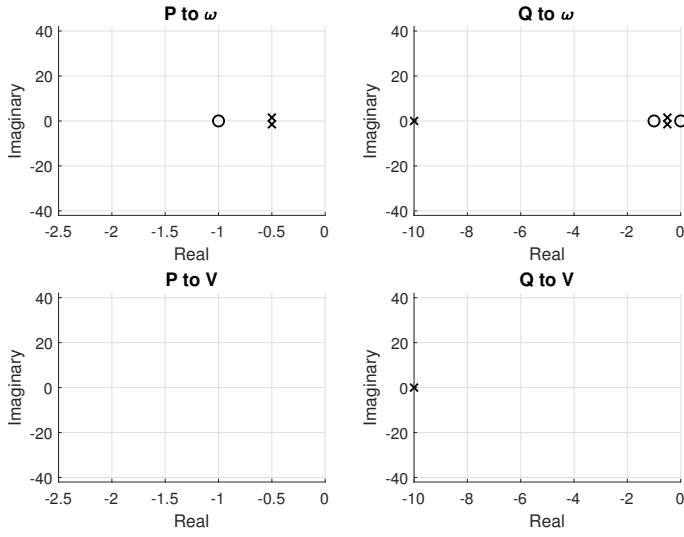


Fig. 8. Pole-zero plots for a modified base case when the VSG parameters perfectly match the SG parameters. (Black: modified base case. Crosses refer to poles, circles indicate zeros.)

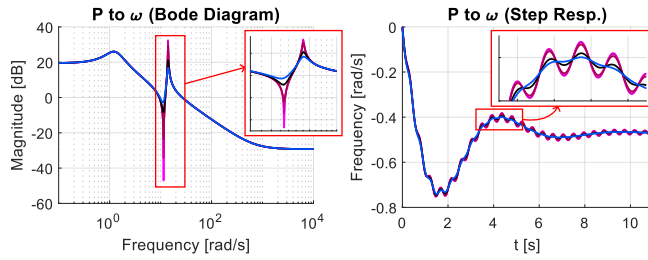


Fig. 9. Bode magnitude plots and step responses of $P \rightarrow \omega$ for $D_v \in [0.3, 34]$ p.u with $H_v = 2H_v^{\text{default}}$ for all. (Black: base case $D_v = 17$ p.u, red: D_v smaller than default, blue: D_v larger than default. Darker shades refer to parameter values closer to the base case.)

Thus, the choice of $K_{q,v}$ should depend on the desired droop level.

E. Sensitivity With Respect to $T_{q,v}$

Fig. 11 shows the Bode plots and step responses of $Q \rightarrow V$ for changing QV-droop time constants in the range $[0.05, 0.2]$ s, where $T_{q,v} = 0.1$ s by default. We observe that $T_{q,v}$ has no effect on $P \rightarrow \omega$. While not easily observed in the figure, $Q \rightarrow V$ contains a second real pole for $T_{q,v} \neq T_{q,s}$, and for smaller lag $T_{q,v}$, a slightly faster convergence of the step response is observed.

F. Sensitivity With Respect to X_v

X_v is varied within $[0.1, 0.4]$ pu, with the nominal value being $X_v = 0.2$ pu. The choice of X_v also affects the operating point of the system, and we recompute it accordingly. The Bode plots of $P \rightarrow \omega$ and $Q \rightarrow V$ are shown in Fig. 12.

While X_v has no effect on the primary poles of $P \rightarrow \omega$, the location of its secondary poles and zeros changes, and the best pole-zero cancellation appears to be achieved for $X_v = X_s$. Hence, matching impedances has significant importance. In the mismatched case, an additional fast real pole appears in

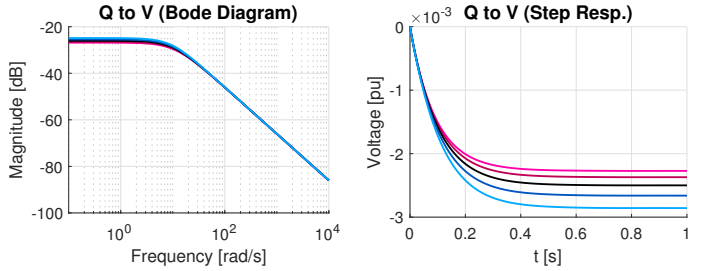


Fig. 10. Bode magnitude plots and step responses of $Q \rightarrow V$ for $K_{q,v} \in [0.05, 0.2]$ pu (Black: base case $K_{q,v} = 0.1$ pu, red: $K_{q,v}$ smaller than default, blue: $K_{q,v}$ larger than default. Darker shades refer to parameter values closer to the base case.)

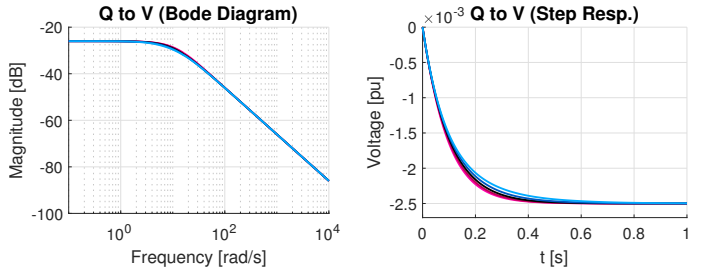


Fig. 11. Bode magnitude plots and step responses of $Q \rightarrow V$ for $T_{q,v} \in [0.05, 0.2]$ s. (Black: base case $T_{q,v} = 0.1$ s, red: $T_{q,v}$ smaller than default, blue: $T_{q,v}$ larger than default. Darker shades refer to parameter values closer to the base case.)

$Q \rightarrow V$, and it becomes slower as X_v increases. But even then, the main difference lies in this transfer function's steady-state value. As expected, the change in voltage magnitude in response to the same step is larger for bigger X_v .

G. Tuning Guidelines

Here, we provide a set of additional numerical tuning guidelines for the VSG in the specific system under consideration based on the analytical models and previous observations:

- Letting $H_v \in [4, 5]$ s ensures a good trade-off between the benefits of matching inertia and having slightly larger inertia.
- Setting $D_v \geq 17$ p.u eliminates the secondary oscillations in $P \rightarrow \omega$.
- Matching $X_v = X_s$, and keeping the XR-ratio of the VSG high are both indispensable.
- Having a governor lag $T_{p,v} \in [0.06, 0.12]$ s is desirable, as much lower values could create further oscillations.
- Finally, QV-droop lag can be lower for the VSG, e.g., $T_{q,v} = 0.05$ s, to have slightly faster convergence.

APPENDIX B SIMULATION CASE STUDIES

This section verifies the analytical model derived in Section III and some of the major observations with simulation case studies. We first explain the simulation setup and implementation to then provide step responses for active and reactive power steps. We vary H_v , X_v , XR-ratio, and the load impedance.

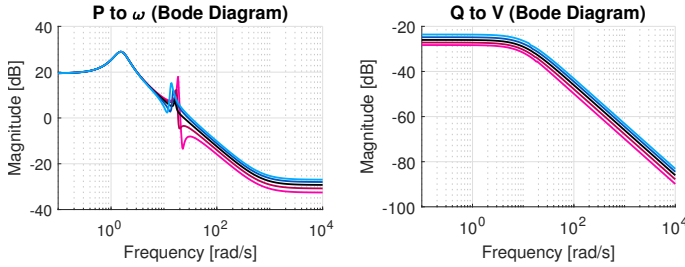


Fig. 12. Bode magnitude plots of $P \rightarrow \omega$ and $Q \rightarrow V$ for $X_v \in [0.1, 0.4]$ pu (Black: base case $X_v = 0.2$ pu, red: X_v smaller than default, blue: X_v larger than default. Darker shades refer to parameter values closer to the base case.)

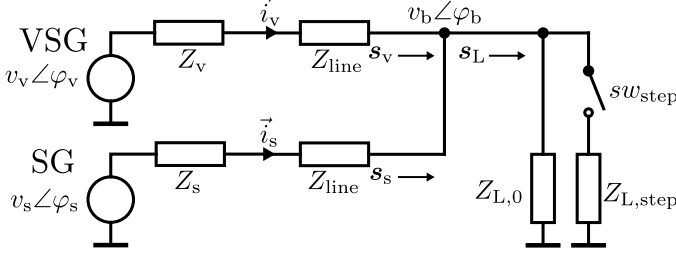


Fig. 13. Diagram of the simulation model.

The system is implemented in MATLAB/Simulink. Fig. 13 shows its diagram. The grid model includes resistive-inductive line impedances. Idealized controlled voltage sources with input signals \vec{v}_v and \vec{v}_s provide the internal voltages, assuming average converter models. The load is modeled by the two impedances $Z_{L,0}$ and $Z_{L,step}$, the values of which are determined to create the operating point and the power step. The step is performed by closing the switch sw_{step} .

Unless later mentioned otherwise, we use the parameters in Table I and the line impedances $Z_{line} = 0.0054 + 0.0076j$ pu, matching [6]. The system is initialized to $s_{v,r} = s_{s,r} = [0.5 \ 0.5]^\top$ pu and the operating point described in Table II. The impedance $Z_{L,step}$ is set to ensure a load step of $\Delta s_L = [0.02 \ 0.02]^\top$ pu.

Power flow matrices \mathbf{K}_v and \mathbf{K}_s depend on the voltage and angle operating points, and due to the line impedances, the real operating points slightly deviate from the precomputed solution of (3) and (4). Hence, the analytical step responses are obtained using the actual operating points obtained from the simulations. Since p_L and q_L are perturbed simultaneously, these simulation studies do not identify $P \rightarrow \omega$ and $Q \rightarrow \omega$ separately. Hence, we focus on the signals $\Delta\omega_s$ and Δv_s .

A. Verification of the Small-Signal Model

Fig. 14 compares the step response computed from the small-signal model to the one obtained from the simulations. The parameters are as described above, and $Z_{L,0} = 0.5 + 0.5j$ pu and $Z_{L,step} = 25 + 25j$ pu accordingly. As Fig. 14 shows, despite a minor mismatch during the transient, the simulation plots closely follow the predictions.

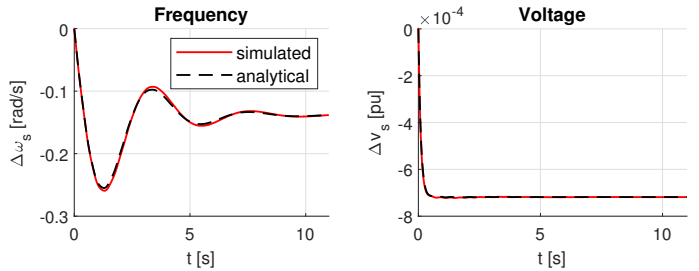


Fig. 14. Comparison of simulated and analytical step responses (base case).

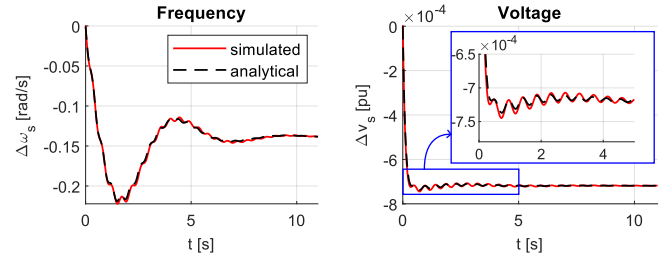


Fig. 15. Comparison of step responses for $H_v = 2H_v^{\text{default}}$.

B. Case Studies for Different Parameter Realisations

We now vary the parameters. First, Fig. 15 shows the case where $H_v = 2H_v^{\text{default}}$. Second, the step responses for $X_v = 1.4X_v^{\text{default}}$ are presented in Fig. 16. Third, Fig. 17 includes a nonzero stator resistance for the VSG: $X_v/R_v = 3$. Finally, we showcase the use of different load impedances in Fig. 18: $s_{v,r} = s_{s,r} = [0.5 \ 0.25]^\top$ pu is chosen, such that $Z_{L,0} = 0.8 + 0.4j$ pu. Furthermore, $\Delta s_L = [0.04 \ 0.04]^\top$ pu yields $Z_{L,step} = 12.5 + 12.5j$ pu. Setpoints, system initialisation, and power flow matrices are adjusted accordingly.

In all cases, the simulations support the analytical results. Fig. 15 shows smaller primary oscillations and stronger secondary oscillations in the frequency step response than in Fig. 14, matching the findings from Section IV-A. Also, stronger secondary oscillations that can be attributed to $P \rightarrow V$ can be observed in the combined voltage step response. Similarly, the slightly stronger oscillations in the frequency step response of Fig. 16 and the larger voltage drop in steady-state due $X_v > X_s$ support the analytical results from Section A-F. As discussed in Section IV-C, due to a low XR-ratio, we can observe stronger secondary oscillations in both, the frequency and the voltage step response of Fig. 17 than in the base case.

In addition to that, Fig. 18 illustrates that simulations and analytical results also match for different loads and power settings. We observe larger perturbations in frequency and voltage due to the bigger load step size.

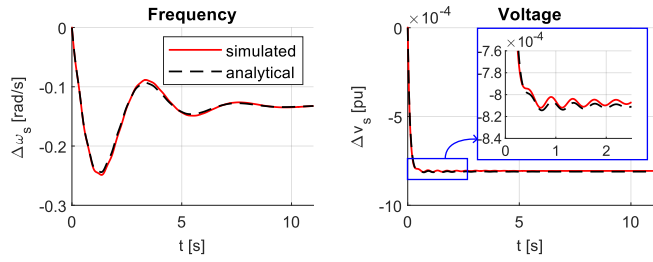


Fig. 16. Comparison of step responses for $X_v = 1.4X_v^{\text{default}}$.

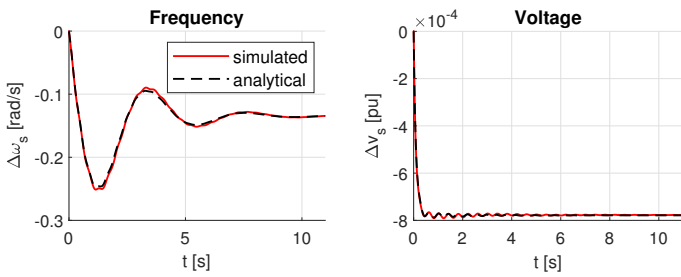


Fig. 17. Comparison of step responses for $R_v \neq 0$ pu such that $X_v/R_v = 3$.

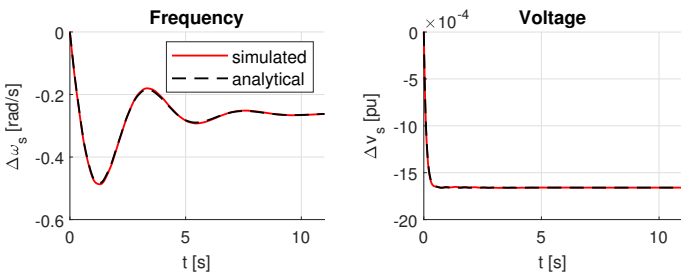


Fig. 18. Comparison of step responses for changed power levels and loads:
 $s_{v,r} = s_{s,r} = [0.5 \ 0.25]^\top$ pu and $\Delta s_L = [0.04 \ 0.04]^\top$ pu, yielding
 $Z_{L,0} = 0.8 + 0.4j$ pu and $Z_{L,\text{step}} = 12.5 + 12.5j$ pu